Simultaneous optimization of lignocellulosic sugar catabolism via systematic laboratory evolution in dynamic conditions

Sunghwa Woo[a,b,1], Hyun Gyu Lim[a,b,c,d,1], Brenna Norton-Baker[e,f], Torrey M. Lind[e,f], Nathan E. Gladden[f,g], Yan Chen[b,h], Thomas Eng[b,h], Christopher W. Johnson[e,f], Aindrila Mukhopadhyay[b,h], Christopher J. Petzold[b,h], Adam M. Guss[f,g], Gregg T. Beckham[e,f], Adam M. Feist[a,b,i,*]

[a]Department of Bioengineering, University of California San Diego, 9500 Gilman Dr., La Jolla, CA 92093, USA

[b]Joint BioEnergy Institute, 5885 Hollis Street, 4th floor, Emeryville, CA 94608, USA

[c]Department of Biological Sciences and Bioengineering, Inha University, Inha-ro 100, Michuhol-gu, Incheon 22212, Korea

[d]Institute of AI-driven Industrial Biotechnology, Inha University, Incheon 22212, Korea

[e]Renewable Resources and Enabling Sciences Center, National Renewable Energy Laboratory, Golden, CO 80401, USA

[f]Agile BioFoundry, Emeryville, CA 94608, USA

[g]Biosciences Division, Oak Ridge National Laboratory, Oak Ridge, Tennessee, United States of America

[h]Biological Systems and Engineering Division, Lawrence Berkeley National Laboratory, Berkeley, CA 94720, USA

[i]Novo Nordisk Foundation Center for Biosustainability, Technical University of Denmark, 2800 Kgs., Lyngby, Denmark

[1]These authors made equal contributions to this work.

[*]Corresponding author, afeist@ucsd.edu

Abstract

Efficient co-utilization of hexose and pentose sugars from lignocellulose is essential for microbial production of bio-based chemicals, yet engineered non-native catabolic pathways can be suboptimal and evolutionarily unstable in complex resource environments. We used a *Pseudomonas putida* strain, previously engineered to catabolize xylose and arabinose to examine how resource abundance, temporal availability, and sub-culturing criteria shape evolutionary outcomes. Using an automated adaptive laboratory evolution (ALE) platform, we evolved the strain under static conditions with single selection pressures and dynamic regimes that imposed selection pressures on multiple sugars. These environments drove divergence between catabolic specialists and generalists. While selection regimes with weak or absent selection for xylose frequently resulted in loss of xylose catabolism, evolution under carbon-limited, mixed-sugar environments promoted stable retention and coordinated optimization of multiple catabolic pathways, increasing total sugar consumption in mixed-sugar conditions. Genomic, proteomic, and biochemical analyses showed that evolutionary stability was determined by pathway-specific fitness costs, leading to either pathway loss or cost-reducing refinement, depending on selection strength. An isolated generalist clone also exhibited improved indigoidine production from mixed sugars when compared to the parental strain. Together, these findings link resource dynamics to fitness landscapes that determine catabolic specialization, generalization, evolutionary trade-offs, and applicability to bioconversion.

Keywords: Adaptive laboratory evolution, evolution dynamics, mixed-sugar utilization, *Pseudomonas putida*, indigoidine, proteomics, whole genome sequencing

Introduction

A major challenge in lignocellulosic bioconversion is enabling microbes to efficiently assimilate mixed sugars under industrially relevant conditions. Lignocellulosic hydrolysates contain both hexoses and pentoses, and biocatalysts must co-utilize these substrates to maximize production yields and rates[1–4]. Recent advances in industrial biotechnology have enhanced the efficiency of microbial biocatalysts for converting biomass feedstock into value-added chemical products[5,6]. Nevertheless, the engineering of such microbes is complex, given the regulatory and metabolic strategies that microbes have evolved to handle fluctuating substrate availability and ecological competition in natural environments[7–9]. As a result, microbial species often exhibit distinct substrate preferences, and hierarchical substrate utilization is governed by mechanisms such as carbon catabolite repression, which promotes rapid growth and competitive dominance by prioritizing preferred substrates[10–12]. While advantageous in natural ecosystems, such regulatory mechanisms hinder the simultaneous assimilation of mixed substrates, which is a critical limitation for microbial biocatalysts designed to process biomass-derived feedstocks[13–15].

Pseudomonas putida has emerged as an attractive microbial host for bioproduction, owing to its stress tolerance and ability to catabolize aromatic compounds[16–18]. Engineering efforts have expanded its substrate range through the introduction of multiple variants of enabling catabolic pathways[19–26]. Building on these advances, the JE3692 strain enabled simultaneous utilization of multiple substrates, including glucose, xylose, arabinose, acetate, and *p*-coumarate, via chromosomal integrated pentose catabolic pathways, adaptive laboratory evolution (ALE), and alleviation of carbon catabolite repression[23]. Despite this progress, fully optimizing the

simultaneous utilization of multiple sugars, especially non-native substrates, remains difficult due to complex regulatory and metabolic interplay.

ALE is a powerful approach to strain optimization that can help overcome strain inefficiencies via diversity generation and selection[27]. Most ALE studies to date have been conducted under static conditions with a single selection pressure[28–33]. Such regimes may not impose sufficient or appropriate selection pressure for performance in mixed-sugar contexts, as catabolic pathways not under direct selection often remain unoptimized. Moreover, heterologous or engineered pathways that reduce fitness can be lost, unless their expression is directly coupled to survival. While some studies have attempted co-optimization under multiple selection pressures within a single ALE campaign, outcomes have typically included either limited fitness improvements compared to single-substrate ALE or the loss of substrate-specific beneficial mutations[34,35]. This underscores the need for alternative ALE strategies that incorporate environmental complexity and dynamics to drive balanced optimization of multiple substrates.

Here, we used an automated ALE platform to evolve the previously engineered *P. putida* strain, JE3692, carrying heterologous xylose and arabinose catabolic pathways[23] under both single-sugar and mixed-sugar regimes. This comparative approach allowed us to probe how environmental composition and temporal dynamics shape evolutionary trajectories in an application-driven context. Multi-omics analyses revealed distinct adaptive strategies, including regulatory rewiring and selective pathway retention. Furthermore, a strain with improved mixed-sugar utilization exhibited enhanced production of the non-ribosomal peptide indigoidine, underscoring the biotechnological potential of evolution-guided strategies. Our findings demonstrate that dynamic ALE can be used to dissect carbon catabolism by revealing how differential substrate utilization rates, pathway-specific fitness costs, and time-varying selection pressures shape evolutionary outcomes, providing design guidelines for engineering microbial platforms for mixed and heterogeneous feedstocks as well as similar complex evolutionary engineering goals.

Results

Systematic dynamic evolution for optimized utilization of the major lignocellulosic sugars

The engineered *Pseudomonas putida* strain JE3692 was used as the starting strain for all ALE campaigns[23]. This strain natively utilizes glucose and was previously modified to catabolize xylose and arabinose, two additional major sugars commonly derived from hemicellulose (**Figure 1A**). This strain harbors two heterologous catabolic pathways: for xylose utilization, the xylose isomerase pathway from *Escherichia coli* includes *xylE*, *xylA*, *xylB*, *tkt*, and *tal*. For arabinose metabolism, the oxidative arabinose pathway includes *araE1* from *E. coli* and *araA2*, *araB2*, *araC2*, *araD2*, and *araE2* from *Burkholderia ambifaria* AMMD[36]. In JE3692 strain, two deletions were introduced: *gcd* (glucose dehydrogenase) was deleted to prevent the formation of gluconate and xylonate[21,37], and *crc* (catabolite repression control protein) was deleted to avoid the native regulation for sugar catabolism[14,25,38]. This strain represented both a promising candidate to build upon for industrial bioprocessing and a relevant test case for exploring dynamic ALE-driven optimization given its combination of native and engineered metabolic capabilities.

The baseline fitness of JE3692 was evaluated in single-sugar and mixed-sugar conditions. The strain exhibited a specific growth rate of 0.42 ± 0.04 h^{-1} in glucose minimal medium, while growth rates in xylose and arabinose minimal media were lower, at 0.20 ± 0.01 and 0.14 ± 0.02 h^{-1}, respectively. In a mixed-sugar minimal medium (4 g/L each), the strain grew at 0.46 ± 0.04 h^{-1}, 23% slower than the previously reported rate (0.60 h^{-1})[23]. These lower growth rates on xylose and arabinose relative to glucose highlight differences in catabolic efficiency among the pathways and motivate further optimization of the heterologous sugar utilization systems[25].

To investigate variation in evolutionary adaptation across different sugar conditions and to enable robust, multi-sugar conversion[34], we performed multiple ALE experiments under both static and dynamic conditions. All ALE experiments were conducted using an automated robotic ALEbot platform, which enabled consistent, systematic, and parallel execution of multiple, independently-controlled evolution lines, thereby minimizing human error[39] (**Figure 1B**). The ALE trajectories were categorized into static and dynamic selection conditions (**Figure 1C**). In static ALE, modified M9 minimal medium was supplemented with 4 g/L of a single sugar, namely glucose (GLC), xylose (XYL), or arabinose (ARA). Dynamic ALE consisted of three regimes: HSM (4 g/L each glucose, xylose, and arabinose) with OD-based transfer; LSM (0.5 g/L each) with sugar depletion-based transfer; and GXA, namely sequential exposure to glucose, xylose, and arabinose (4 g/L each). While GXA introduces dynamic selection through explicit sequential sugar exposure, the mixed-sugar conditions (HSM and LSM) are also dynamic in that differential utilization rates of glucose, xylose, and arabinose lead to temporal shifts in substrate availability and selection pressure within each growth cycle. Each ALE condition was performed in quadruplicate, yielding 24 independent lineages.

ALE experiments were executed until growth improvements plateaued in at least three of the four replicates per condition. Across the approximately 3-month experiments, cultures underwent 63–109 passages, corresponding to 394–709 generations and $32.4–61.5 \times 10^{11}$ cumulative cell divisions (CCDs) (**Supplementary Table 1**)[40]. Growth rate improvements were typically observed early and tended to stabilize after 34–55 passages (**Supplementary Figure 1**). Clonal isolates were obtained from all end-point populations for phenotypic and genotypic

133 characterization, as they were expected to exhibit distinct captive fitness depending on their
134 respective selection regimes (**Figure 1D**).

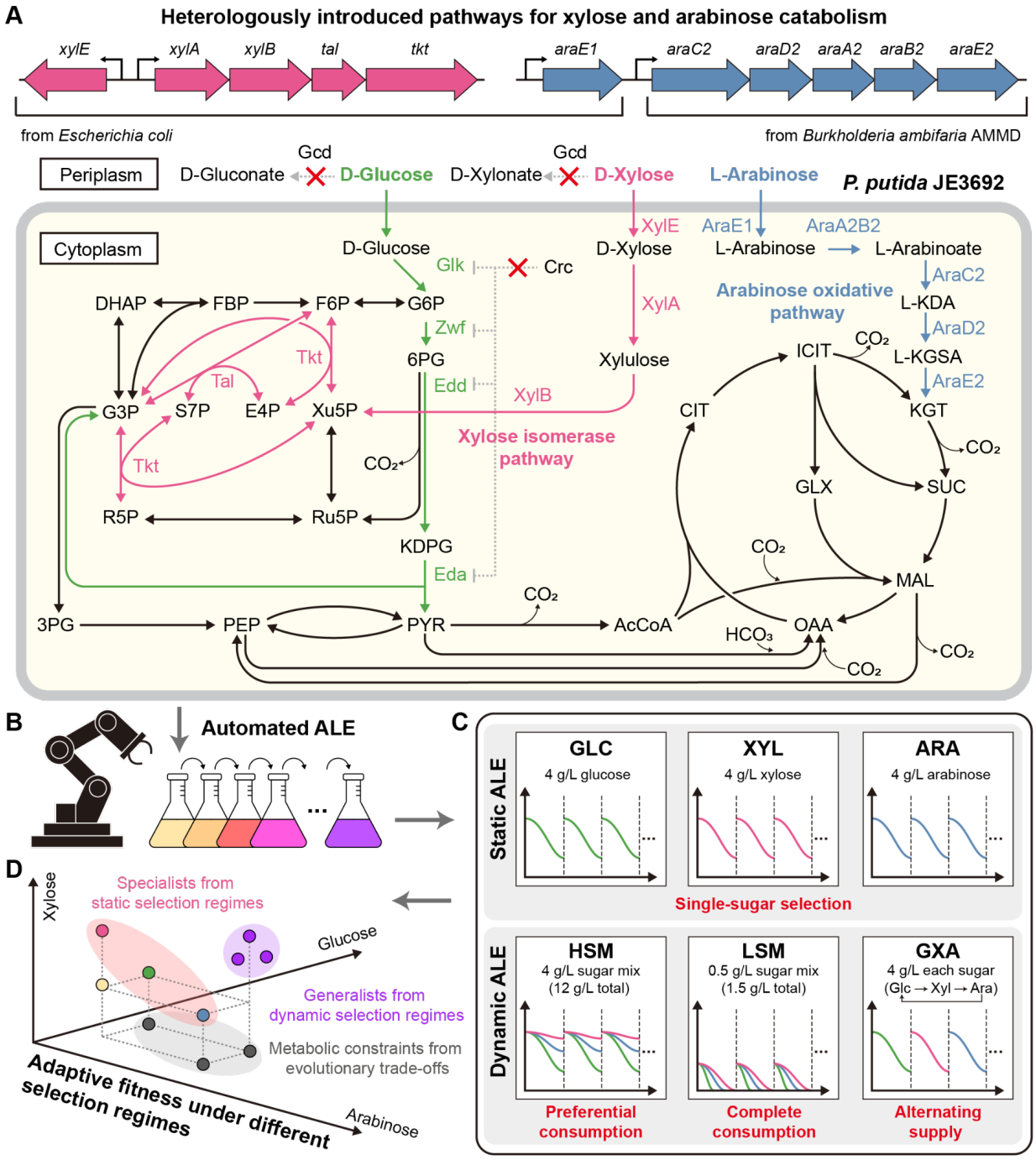

135

136 **Figure 1. Systematic dynamic evolution for optimized utilization of multiple sugars**

137 **(A)** Catabolic pathways for glucose, xylose, and arabinose in JE3692. Genes for each pathway are
138 highlighted with a different color: green, endogenous Entner-Doudoroff (ED) pathway; pink,
139 heterologous xylose isomerase pathway; blue, heterologous arabinose oxidative pathway. Gray

dotted lines and red crosses indicate the deleted genes (*gcd* and *crc*). Abbreviations: G6P, D-glucose 6-phosphate; 6PG, D-gluconate 6-phosphate, KDPG, 2-dehydro-3-deoxy-D-gluconate 6-phosphate; F6P, D-fructose 6-phosphate; FBP, D-fructose 1,6-bisphosphate; DHAP, dihydroxyacetone phosphate; G3P, D-glyceraldehyde 3-phosphate; 3PG, 3-phospho-D-glycerate; PEP, phosphoenolpyruvate; PYR, pyruvate; AcCoA, acetyl-CoA, CIT, citrate; ICIT, isocitrate; KGT, 2-ketoglutarate; SUC, succinate; MAL, malate; OAA, oxaloacetate; GLX, glyoxylate; X5P, xylulose 5-phosphate; Ru5P, ribulose 5-phosphate; R5P, ribose 5-phosphate; E4P, D-erythrose 4-phosphate; S7P, D-sedoheptulose 7-phosphate; L-KDA, 2-keto-3-deoxy-L-arabinose; L-KGSA, 2-ketoglutarate semialdehyde. **(B)** Automated ALEbot robotic platform, which enabled consistent, systematic, and parallel execution of multiple independently controlled evolution lineages, thereby maximizing consistency. **(C)** ALE strategies used in this study. Static ALE groups: GLC (glucose 4 g/L), XYL (xylose 4 g/L), ARA (arabinose 4 g/L). Dynamic ALE groups: HSM (glucose 4 g/L, xylose 4 g/L, and arabinose 4 g/L; selective sugar consumption allowed), LSM (glucose 0.5 g/L, xylose 0.5 g/L, and arabinose 0.5 g/L; complete sugar consumption mandated), GXA (glucose 4 g/L, xylose 4 g/L, or arabinose 4 g/L; each sugar alternatively supplied in series). Each ALE was performed with four replicates (n = 4). The differently colored curves in the simplified graph represent the expected sugar consumption profiles for each passage, separated by dotted lines: green for glucose, pink for xylose, and blue for arabinose. **(D)** A conceptual diagram of the fitness landscape highlighting potential evolutionary outcomes. Selected phenotypes may range from catabolic specialists, optimized for catabolism of a specific substrate but often incurring trade-offs on others, to catabolic generalists, which utilize a range of targeted metabolites without significant trade-offs on any one substrate.

Static ALE selected for substrate-specific catabolic adaptation and trade-offs in unselected functions

The specific growth rates of evolved isolates from the static ALEs were compared to assess their fitness improvements on each sugar. The GLC isolates showed an insignificant increase in growth rate in glucose minimal medium ($p > 0.05$) (**Figure 2A**). The highest growth rate was 0.56 h^{-1}, about 66% of that reported for evolved wild-type *P. putida* populations (0.85 h^{-1})[41], likely reflecting disruption of the gluconate branch of glucose catabolism (*gcd* gene deletion). The XYL and ARA isolates exhibited improved growth when cultured in their respective selection conditions. Specifically, the growth rates improved by up to 1.5-fold for xylose (0.29 h^{-1}) and 4.1-fold for arabinose (0.60 h^{-1}) (**Figure 2B-C**), suggesting that adaptive mutations in the corresponding sugar catabolic pathways were acquired during evolution.

Beyond condition-specific improvements, notable unexpected impacts on alternative sugar catabolism were also observed. Notably, three GLC (1, 2, 4) and one ARA (1) isolates failed to grow on xylose, suggesting an inactivation of the heterologous xylose pathway (*vide infra*, **Figure 2A, C**). Meanwhile, several GLC isolates exhibited enhanced growth on alternative sugars, particularly arabinose. Namely, the GLC1 and GLC4 strains showed elevated growth in arabinose medium, despite arabinose not being included in their original selection regime (**Figure 2A**). All statically evolved isolates showed no significant improvement in growth rate in HSM medium (4 g/L each of glucose, xylose, and arabinose), indicating that sugar-specific adaptations may not translate into improved fitness in mixed environments and motivating alternative ALE approaches (**Supplementary Figure 2**).

183 To identify genetic changes associated with the observed physiology, whole-genome sequencing
184 was performed on the statically evolved isolate, revealing key mutations that enhanced fitness on
185 xylose and arabinose, and no mutations were identified in the glucose catabolic pathway of the
186 GLC1-4 strains, consistent with no significant improvement in growth rate in glucose medium.
187 Recurrent mutations were observed within each lineage: the XYL strains consistently carried
188 mutations in only *xylB*, whereas the Ara strains shared mutations in *araD2*, *araC2*, *araE1*, or their
189 intergenic region (**Figure 2D**). Additionally, a native gene, PP_3603 encoding a transcriptional
190 regulator of the glucuronate and glucarate catabolic pathways, was also mutated across ARA
191 isolates, suggesting its involvement in arabinose catabolism.

192 We also identified endogenous genes that were repeatedly mutated across multiple statically
193 evolved lineages, indicating convergent adaptation. Of the 28 mutations identified in regions
194 repeatedly mutated across independent lineages, 12 mapped to functional genes, including
195 PP_1650 (GacS, a two-component histidine kinase), PP_4171 (hypothetical protein), PP_4173
196 (two component sensor histidine kinase/response regulator), and PP_4373 (FleQ, a transcriptional
197 regulator) (**Supplementary Figure 3**). We interpret these changes as generally beneficial
198 adaptations to laboratory environments, based on their convergence across multiple ALE groups
199 and observed occurrence in previous ALE studies with *P. putida* KT2440[41–43].

200 The *xylB* gene emerged as a common target wherein mutations either improved or impaired cellular
201 fitness on xylose (**Supplementary Figure 4**). Mutations in *xylB* of the XYL1-4 strains occurred
202 at amino acids 395 and 396 (**Figure 2D**), which are highly conserved residues in XylB homologues
203 (**Supplementary Figure 5)**. Disruptive *xylB* mutations included a frameshift (GLC4) and a
204 premature stop codon (ARA1). The other isolates incapable of xylose catabolism exhibited an
205 identical insertion mutation in the intergenic region between *xylE* and *xylA*, potentially reducing
206 expression of the downstream xylose transporter and catabolic enzymes. Interestingly, these two
207 divergent mutational strategies in the xylose pathway revealed the emergence of catabolic
208 specialists and the trade-offs associated with a functional loss not under selection during the
209 evolution experiments.

210 Interestingly, compared to the xylose pathway, no disruptive mutations were found in the arabinose
211 pathway (**Figure 2D**). This distinction is important because both pathways are heterologous, yet
212 only one appears to be more favored. All 8 observed mutations in this pathway were found
213 exclusively in ARA isolates: 3 occurred in the intergenic region upstream of the *araCDAB2* operon,
214 and 5 were in the N-terminal region of the *araC2* or *araD2* genes, all which were likely involved
215 in regulating expression levels[44]. Strains with these mutations exhibited significantly increased
216 growth rates in arabinose minimal media. Additionally, 3 mutations in the PP_3603 gene likely
217 enhanced arabinose catabolism by modulating the expression of PP_3602, which shares the same
218 functional annotation as the *araE2* gene (2-ketoglutarate semialdehyde dehydrogenase)[45,46].
219 Collectively, the phenotyping and genomic analysis of the statically evolved strains showed trends
220 of condition-specific optimization and generation of catabolic specialists with no significant
221 improvement of growth on sugar mixtures ($p > 0.05$).

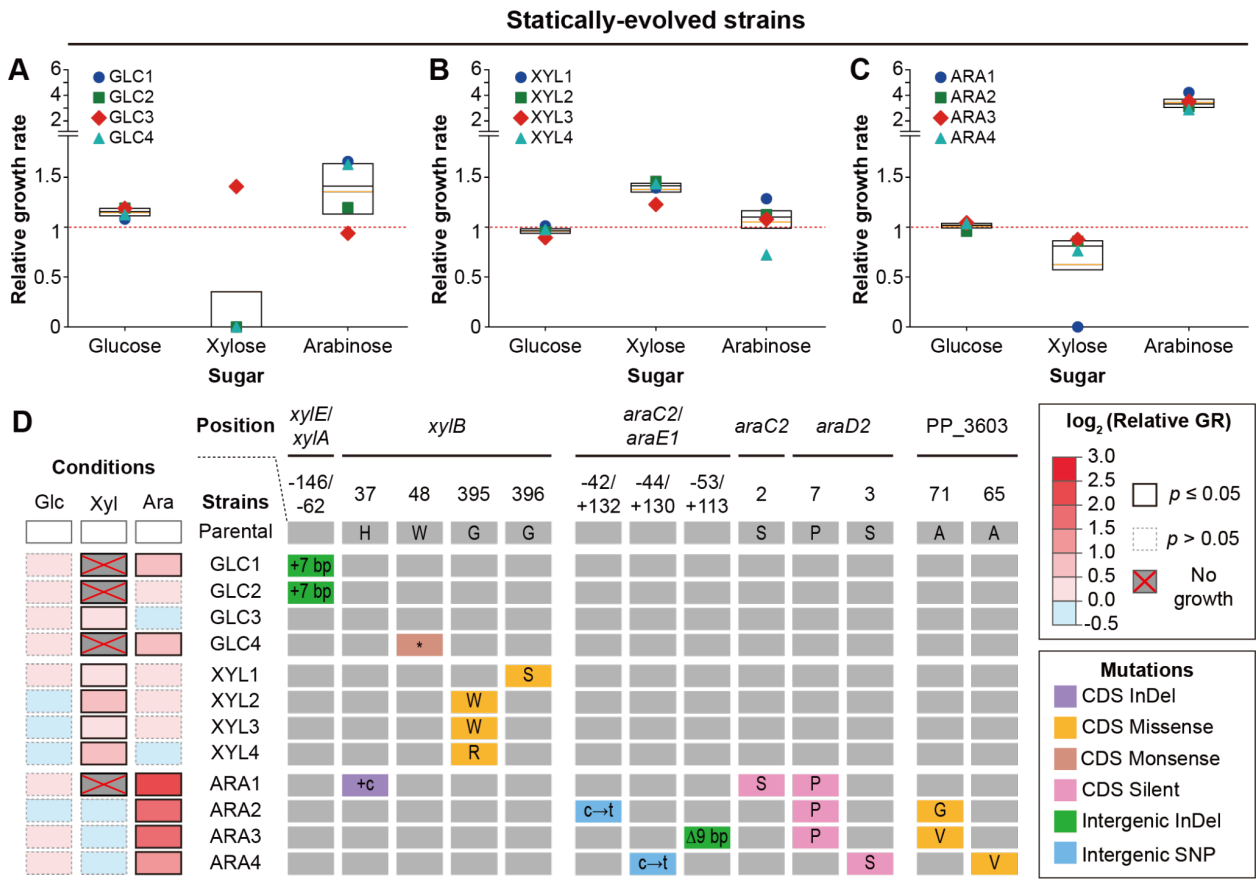

Figure 2. Sugar-specific adaptations and trade-offs in statically evolved strains

Box plots show the relative growth rates of statically evolved strains isolated from **(A)** GLC, **(B)** XYL, and **(C)** ARA conditions under single-sugar conditions (glucose, xylose, and arabinose), compared to the starting JE3692 strain. Each dot represents the mean fold change in specific growth rate from duplicates ($n = 2$). Each box indicates the interquartile range, and each black and orange solid line in the box indicates the median and mean value, respectively. Red dotted lines indicate a fold change of 1. The *x*-axis represents sugar conditions under which the isolates were grown, and the *y*-axis represents the specific growth rate (h^{-1}). **(D)** Detailed mutational analysis related to xylose and arabinose catabolism in statically evolved strains. The right side shows mutations in the heterologous xylose and arabinose catabolic pathways. Rows and columns represent isolates and mutational positions, respectively. Uppercase and lowercase letters in boxes indicate amino acids and nucleobases, respectively. Different colors represent different mutation types detailed in the legend. The heatmap on the left shows the log fold change in the specific growth rate of each evolved isolate compared to the parental strain under various sugar conditions, generated from the same dataset as Figure 2A-C. The rows and columns represent isolate and sugar conditions under which the isolates were grown, respectively. Boxes with the color scale represent a gradient according to the log fold change in the specific growth rate (relative GR), showing a range of minimum (light blue) to maximum (red), and gray boxes marked with cross indicate no growth.

242 **Dynamic ALE revealed the selection of catabolic generalists dependent on experimental**
243 **design**

244 The dynamic ALE also enabled generation of both metabolic specialists and catabolic generalists,
245 shaped by their specific selection regimes. As observed for the GLC and ARA statically evolved
246 isolates, the HSM isolates, which did not require complete sugar consumption, selectively lost the
247 ability to grow on xylose as the sole carbon source (**Figure 3A**), indicating that the xylose pathway
248 is detrimental under these conditions. Two HSM isolates showed higher growth rates on arabinose
249 alone whereas their growth rates on glucose alone remained similar to the unevolved parent.
250 Conversely, the LSM and GXA isolates displayed enhanced growth rates on xylose, indicating
251 xylose catabolism was beneficial in these conditions (**Figure 3B-C**). Evolution under the LSM
252 condition also greatly enhanced the growth rate on arabinose, up to 3.0-fold, comparable to the
253 growth rates of the ARA isolates. In contrast, the growth rates on arabinose alone of the GXA
254 isolates were not significantly increased (**Figure 3C**).

255 Growth and sugar consumption of the dynamically evolved strains were also evaluated under the
256 mixed-sugar conditions containing 4 g/L each of glucose, xylose, and arabinose, identical to the
257 HSM selection regime. Consistent with faster growth on individual sugars, the LSM isolates
258 displayed generally higher growth rates than the other isolates. Among these, the LSM1 strain
259 exhibited the highest growth rate (0.65 h^{-1}), 1.4 times that of the JE3692 strain (**Figure 3D**).
260 Moreover, during the exponential growth phase, the LSM isolates generally exhibited higher total
261 sugar consumption rates than the other isolates (**Figure 3E**). Among them, the LSM1 strain
262 showed the highest total sugar consumption rate of 0.46 g/L/h, which was 1.3-fold higher than that
263 of the JE3692 strain. Its glucose consumption rate was comparable to that of JE3692, whereas the
264 consumption rates for xylose and arabinose were 1.9- and 1.3-fold higher, respectively. Meanwhile,
265 consistent with their inability to grow on xylose, the HSM isolates failed to consume xylose under
266 mixed-sugar conditions. These results suggest that the requirement of complete consumption of
267 all three sugars under the LSM condition was effective in simultaneously optimizing catabolism
268 of lignocellulosic sugar mixes.

269 Genome resequencing of the dynamically evolved strains identified the mutations that occurred
270 during evolution (**Figure 3F**). Firstly, a number of isolates carried mutations related to generally
271 beneficial adaptation to laboratory environments, including mutations in PP_1650, PP_4171,
272 PP_4173, and PP_4373, similar to those observed in statically evolved strains (**Supplementary**
273 **Figure 3**). All the HSM isolates, which did not consume xylose, acquired large deletions in the
274 *xylE-xylAB* region (HSM1, HSM3, HSM4) or an insertion upstream of *xylA* (HSM2), presumably
275 leading to the observed elimination of xylose catabolism. In contrast, the LSM and GXA isolates,
276 which retained the ability to utilize all three sugars, acquired non-disruptive mutations, defined
277 here as sequence changes that did not result in loss-of-function, including substitutions or an in-
278 frame deletion. In the arabinose pathway, mutations were identified in the protein sequences of
279 *araE1* and *araC2*, as well as in the intergenic region upstream of *araC2*. However, mutations in
280 *araE1* appeared to have no significant impact on fitness in arabinose medium (**Figure 3F**). The
281 exclusive occurrence of disruptive mutations in the xylose pathway, but not in the arabinose
282 pathway, suggested distinct fitness constraints and motivated the hypothesis that the xylose
283 isomerase pathway imposes a higher fitness cost (*vide infra*) (**Supplementary Figure 3)**.

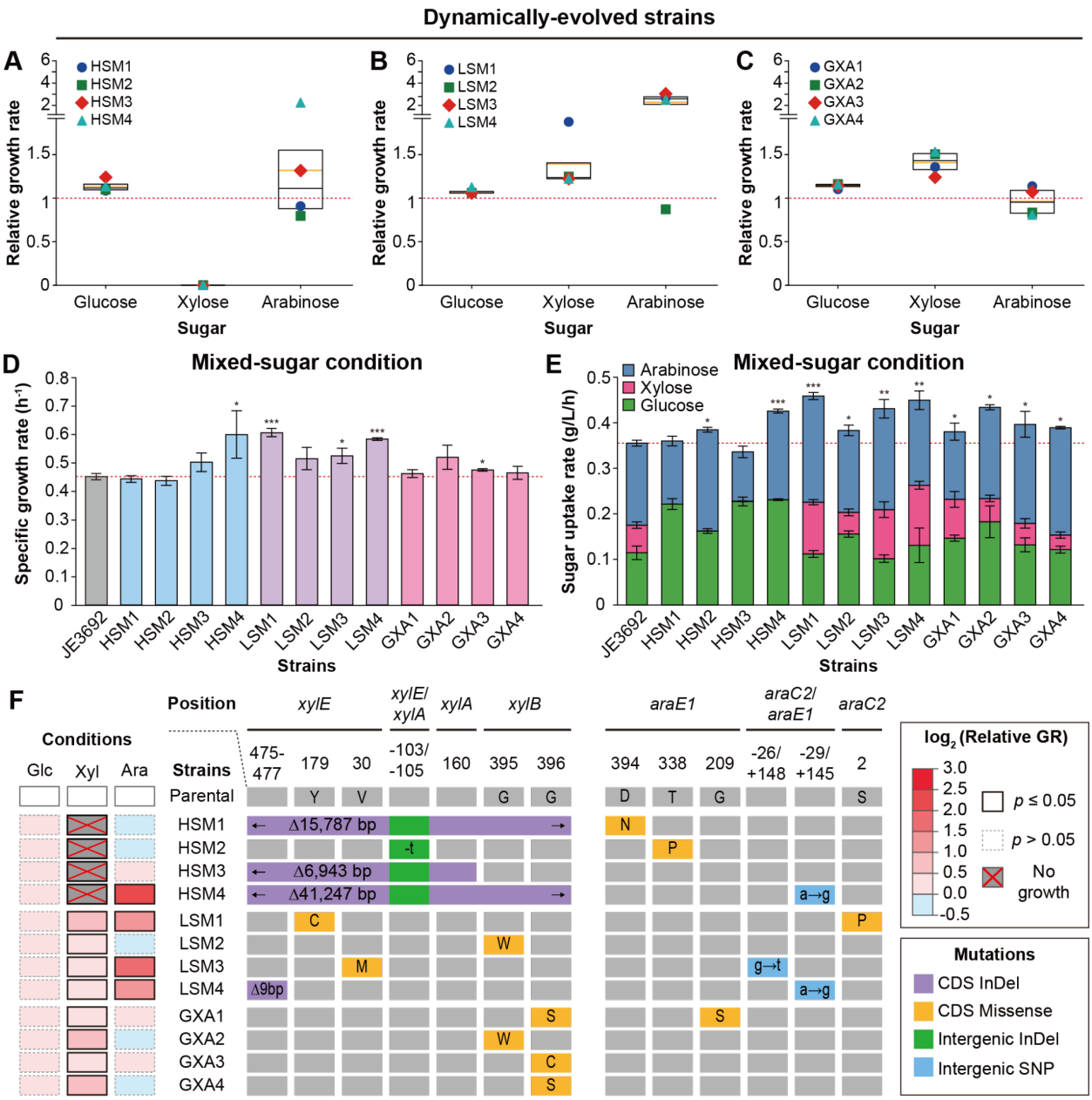

Figure 3. Dynamic selection resulted in the generation of catabolic generalists or strains with trade-offs dependent on media conditions.

Box plots show the relative growth rates of dynamically evolved strains isolated from **(A)** HSM, **(B)** LSM, and **(C)** GXA conditions under single-sugar conditions (glucose, xylose, and arabinose), compared to the parental strain, JE3692. Each dot represents the mean fold change in specific growth rate from duplicates ($n = 2$). **(D)** Specific growth rates of dynamically evolved strains under the HSM mixed-sugar conditions. The *x*- and *y*-axes indicate strains and specific growth rate (h^{-1}), respectively. The gray, light blue, lavender, and pink boxes represent JE3692, HSM, LSM, and GXA isolates, respectively. **(E)** Sugar uptake rates of dynamically evolved strains under the HSM mixed-sugar conditions. The *x*- and *y*-axes indicate strains and sugar uptake rate (g/L/h), respectively. The green, pink, and blue boxes represent glucose, xylose, and arabinose,

respectively. Cultures were conducted in biological triplicates (n = 3). Red dotted lines indicate the specific growth rate and total sugar uptake rate of the JE3692 strain. Error bars indicate the standard deviations. *, **, and *** indicate $p < 0.05$, $p < 0.01$, and $p < 0.001$, respectively. Bars without asterisks represent values that are not statistically significantly different from those of the JE3692 strain. **(F)** Detailed mutational analysis related to xylose and arabinose catabolism in dynamically evolved strains. All other details are the same as those described for Figure 2D.

Evolutionary stability of heterologous sugar catabolism under divergent selection regimes

To assess the causal effects of key non-disruptive ALE-derived mutations, we reverse-engineered several genetic changes back into the parent JE3692 strain and assessed fitness changes under xylose and arabinose conditions. In the xylose pathway, we selected *xylB* G395W, the most convergent mutation in the xylose pathway, and *xylE* Y179C, identified in the LSM1 strain. In the arabinose pathway, we selected *araC2* S2P, identified in the LSM1 strain, *araD2* P7P, the most convergent mutation in the arabinose pathway, and PP_3603 A71V, one of the mutations observed in the ARA isolate. Except for PP_3603 A71V, these mutations independently increased growth rates under the corresponding conditions (**Figure 4A**). Although introducing PP_3603 A71V alone reduced the growth rate on arabinose, it eliminated the initial lag phase, which may explain its persistence during the ALE experiments (**Supplementary Figure 6**). Moreover, evolved strains carrying mutations in PP_3603 (ARA 2–4) also harbored mutations in *araC2* or *araD2* (**Figure 2D**), suggesting that these mutations may modulate the effect of the PP_3603 A71V mutation on growth, although their synergistic effects are not clear.

In a separate assay, to understand the reason for the selective disruption of the xylose pathway during ALE, we examined whether the expression of the xylose and arabinose pathways imposed fitness costs under non-selective regimes using phenotypic assays. To this end, we cultivated the JE3692 and its intermediate strains in glucose minimal medium (**Figure 4B**). The strains utilized were JE212, which lacks both the xylose and arabinose pathways; JE3226, which contains only the xylose pathway; and JE3285, which contains both pathways. All three intermediate strains possessed an intact *crc* gene, which was deleted in the JE3692 strain. The JE3226 strain exhibited a 19% lower growth rate (0.45 ± 0.01 h^{-1}, $p < 0.01$) compared to the JE212 strain (0.56 ± 0.05 h^{-1}). Although the JE3285 strain showed a slightly lower growth rate (0.41 ± 0.01 h^{-1}) than the JE3226 strain (a 9% decrease), the difference was not statistically significant ($p > 0.05$). We also observed a transient accumulation of up to 0.5 g/L fructose in the JE3226 culture grown in glucose minimal medium, whereas only negligible levels were detected in the JE212 culture (**Figure 4C**). Taken together, these results demonstrated that the xylose pathway reduced growth fitness under non-selective conditions, consistent with its selective loss during ALE in the absence of direct selection pressures.

To determine whether non-specific enzymatic activities of the xylose catabolic enzymes contributed to fitness costs and pathway instability during ALE[19,47–49], we examined the biochemical activities of core enzymes, XylA and XylB, using *in vitro* enzyme assays (**Figure 4D**). In the XYL, LSM, and GXA groups, at least one isolate from each carried a substitution at residue 395 of XylB, and thus we compared the activities of the mutant XylB variants (G395R and G395W) (**Figure 2D** and **3F**). In *in vitro* enzyme assays, wild-type XylB exhibited high activity on D-xylulose and even retained background ATPase activity in the absence of a substrate (**Figure 4E**), consistent with previous studies[19,48]. Interestingly, the G395R and G395W variants exhibited markedly reduced xylulose activity, by 37-fold and 330-fold, respectively, despite having evolved

340 under xylose-selective conditions. They also decreased background ATPase activity by 9.9- and
341 5.7-fold, respectively. Analysis of the AlphaFold-predicted structure suggested that residues 395
342 and 396 are positioned adjacent to the ATP-binding region (**Supplementary Figure 7**), suggesting
343 that these substitutions may alter ATP binding affinity[50]. Although the background ATPase
344 activity of wild-type XylB was only about 0.15% of that observed with D-xylulose, its high
345 expression level may increase ATP turnover in the absence of xylose, potentially contributing to
346 the impaired growth (**Figure 4B**). This outcome suggested that maximizing enzyme activity was
347 not the primary determinant of fitness under selection. Accordingly, under strong selection
348 pressure for xylose utilization (XYL, LSM, and GXA), XylB activity appeared to be fine-tuned
349 while ATPase activity was reduced. In contrast, under weaker xylose selection pressure (GLC,
350 ARA, and HSM), evolution tended to disrupt XylB or the entire xylose pathway.

351 The non-specific isomerase activity of XylA toward D-glucose may also influence fitness in this
352 context. Proton NMR analysis qualitatively confirmed that XylA exhibited isomerase activity
353 toward all three target sugars; high for D-xylose, moderate for D-glucose, and minimal for L-
354 arabinose (**Supplementary Figure 8**)[47,49]. This activity toward glucose explains the transient
355 accumulation of fructose in the JE3226 culture (**Figure 4C**). The formation of an inefficient side
356 branch via unnecessary D-fructose production, accompanied by flux imbalance and diauxic sugar
357 utilization[51,52], may have imposed selective pressures to eliminate XylA during ALE
358 experiments[53,54]. Further support comes from the observation that the JE3692 strain showed a 1.9-
359 fold lower growth rate when grown on D-fructose than on D-glucose, likely due to the absence of
360 phosphofructokinase (**Figure 4B**). This may explain why, in ALE regimes with strong selection
361 pressure on glucose catabolism (GLC and HSM), not only XylB but the entire xylose pathway was
362 disrupted by large deletions or mutations in intergenic regions.

363 In another drill-down assay on ALE-derived findings, proteomic analysis suggested that the high
364 protein abundance of XylA and XylB may exacerbate the fitness burden imposed by the xylose
365 isomerase pathway. XylB accounted for 2% and XylA for 0.8% of the total protein by mass
366 (**Figure 4F**). Notably, the protein abundance of XylB was comparable to the total abundance of
367 arabinose catabolic enzymes, and even exceeded that of the three most highly expressed
368 endogenous proteins: TufB (elongation factor Tu-B), GroL (chaperonin), and GtsA
369 (mannose/glucose ABC transporter substrate-binding protein) (**Supplementary Data 2**). These
370 quantitative proteomic patterns indicate that high protein abundance of XylA and XylB amplified
371 their non-specific activities and, in turn, the likely burdensome effects.

372 Finally, to investigate the arabinose pathway, we focused on the AraC2 S2P mutation and its
373 associated proteomic changes in the LSM1 strain. Notably, comparative proteomic analysis
374 revealed that AraC2 abundance in the LSM1 strain was 3.5-fold higher than in the JE3692 strain,
375 due to the S2P mutation (**Figure 4F**). Furthermore, downstream arabinose catabolic enzymes,
376 including AraD2, AraA2, AraB2, and AraE2, also showed increased protein abundance. These
377 increases were likely attributable to a mutation near the 5′ end of *araC2* that destabilized the
378 mRNA secondary structure around the ribosome-binding site, thereby improving ribosome
379 accessibility and translation efficiency (**Figure 4G**)[55]. Indeed, based on UTR Designer
380 predictions[44], the mutant *araC2* was expected to show a 3.4-fold increase in expression.

381 Collectively, these findings demonstrated that evolutionary stability of heterologous pathways is
382 determined by the balance between selection pressure and pathway-specific fitness costs. The
383 arabinose pathway, which imposed minimal fitness burden, was stably retained across conditions.

In contrast, the xylose pathway incurred substantial fitness costs and was therefore maintained only under regimes with strong selection for xylose utilization, where evolution favored mutations that reduced these costs rather than maximizing catalytic activity.

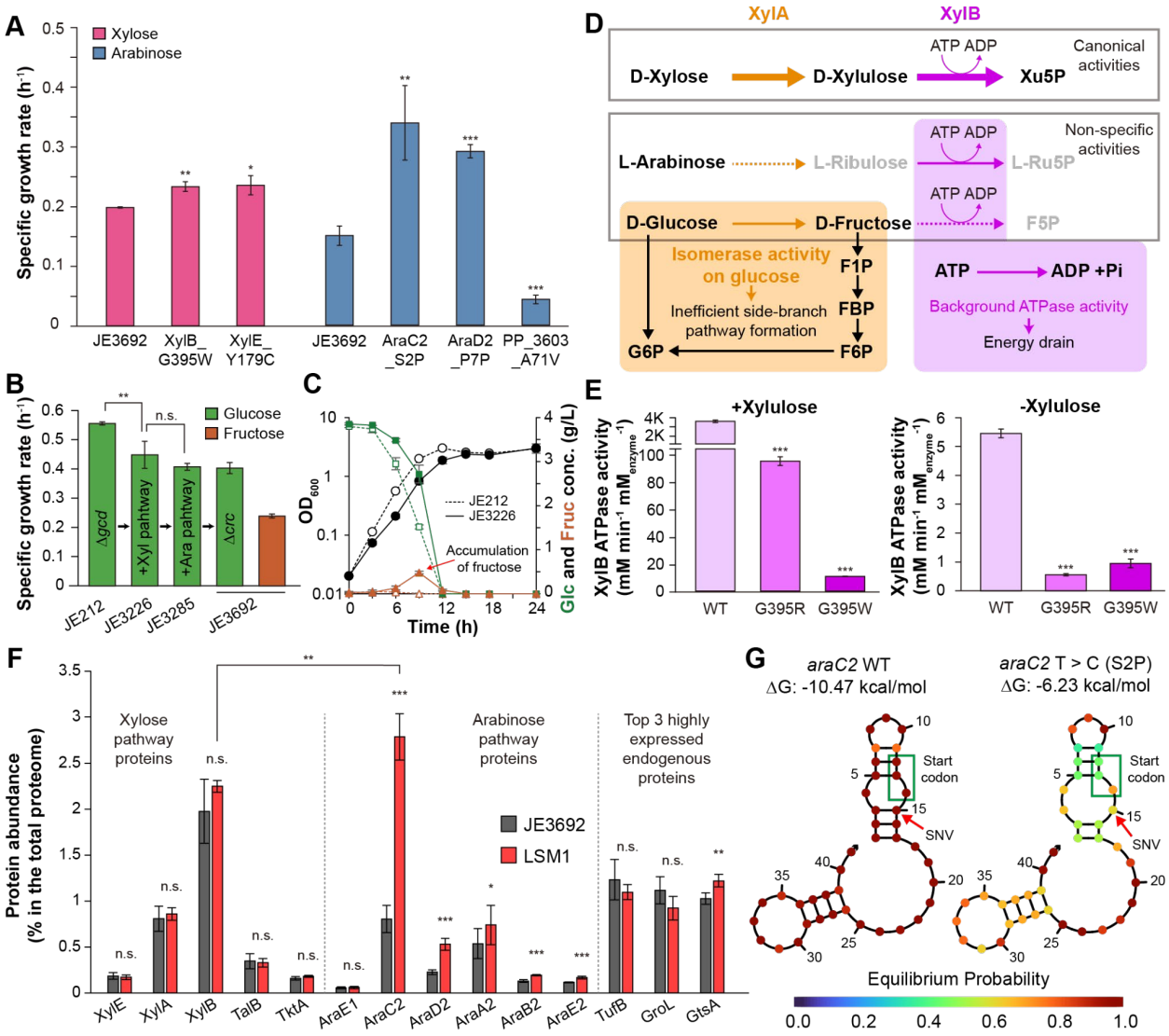

Figure 4. Evolution of heterologous sugar catabolism under divergent selective regimes

(A) Specific growth rates of JE3692 and reverse engineered strains cultured in xylose (pink) and arabinose (blue) minimal media. The *x*- and *y*-axes represent strains and specific growth rate (h^{-1}), respectively. **(B)** Specific growth rates of the JE3692 and its intermediate strains cultured in glucose (green) and fructose (brown) minimal media. The *x*- and *y*-axes represent strains and specific growth rate (h^{-1}), respectively. **(C)** Detailed culture profiles of JE212 (dotted lines and open symbols) and JE3226 (solid lines and closed symbols) in glucose minimal media. Data are from the same dataset as in panel B. The left and right *y*-axes indicate cell biomass (OD_{600}) and concentration of glucose and fructose (g/L), respectively; the *x*-axis indicates time in hours (h). Symbols: black circles, OD_{600}; green squares, glucose; brown triangles, fructose. **(D)** Overview of the proposed evolutionary scenario underlying the negative selection of xylose pathway enzymes.

Orange and purple boxes and arrows indicate enzymatic activities of XylA and XylB, respectively. **(E)** *In vitro* comparison of ATPase activity between wild-type and mutant XylBs in the presence and absence of D-xylulose. Light, regular, and dark purple bars indicate wild type, G395R, and G395W, respectively. The *y*-axis represents ATPase activities (mM/min per mM enzyme), measured via NADH oxidation coupled to pyruvate kinase and lactate dehydrogenase reactions. **(F)** Comparison of the protein abundance levels of heterologous proteins for xylose and arabinose catabolism in JE3692 and LSM1. The *x*- and *y*-axes represent protein and the fraction in the total proteome, respectively. The gray and red boxes represent JE3692 and LSM1, respectively. **(G)** Comparison of secondary structure of 5'- end of mRNA of the wild-type and mutant *araC2*, predicted by NUPACK[55]. Modified base and start codon are highlighted by red circle and green box, respectively. Cultures and enzyme assay were conducted using biological triplicates ($n = 3$), and proteomic analysis was conducted using biological quadruplicates ($n = 4$). Error bars indicate the standard deviations. *, **, ***, and n.s. indicate $p < 0.05$, $p < 0.01$, $p < 0.001$, and $p > 0.05$, respectively. Asterisks without brackets indicate statistical significance compared to the parent.

An evolved isolate with a generalist sugar catabolism enhances indigoidine production

The potential of the evolutionarily optimized LSM1 strain evolved under dynamic conditions as a production host for conversion of lignocellulosic sugars was evaluated using indigoidine production, a natural blue pigment with various industrial applications, as a relevant bioproduct. To achieve this, we introduced the biosynthetic pathway for indigoidine into both the parental strain and the LSM1 strain (**Figure 5A**)[56–59]. This heterologous pathway included the *bpsA* gene encoding blue pigment synthetase A from *Streptomyces lavendulae* and the *sfp* gene encoding 4′-phosphopantetheinyl transferase from *Bacillus subtilis*[60,61]. Using the plasmid system, these two genes were expressed under the *tac* promoter without *lacI*, which has previously been used for strong and constitutive expression in *P. putida* KT2440[62,63]. This plasmid was transformed into JE3692 and LSM1, and the resulting strains, JE3692_IND and LSM1_IND, were cultivated in isotonic sugar media containing 4 g/L each of glucose, xylose, and arabinose, as well as in hydrolysate mimicking sugar media simulating lignocellulosic sugar composition, which contained 24 g/L of glucose, 12 g/L of xylose, and 4 g/L of arabinose[64].

The LSM1_IND strain demonstrated a consistently higher indigoidine titer compared to the JE3692_IND strain (**Figure 5B**). Under isotonic conditions, the LSM1_IND strain produced 1.8 g/L of indigoidine over 48 hours, 1.5-fold higher compared to the JE3692_IND strain under the same conditions. When grown on mock hydrolysate, the LSM1_IND strain achieved a titer of 4.2 g/L over 96 hours, 1.2-fold higher compared to the JE3692_IND strain. This titer improvement was likely due to increased xylose and arabinose catabolism and metabolic flux redistribution described in the previous sections. Specifically, the efficient and direct supply of 2-ketoglutarate, resulting from enhanced arabinose catabolism, likely played a crucial role in increasing indigoidine production. The difference in titer between the two strains was more pronounced in the early stages of cultivation, with the LSM1_IND strain exhibiting 6.9-fold and 5.2-fold higher titers than the JE3692_IND strain after 12 hours under isotonic and mock hydrolysate conditions, respectively. These results demonstrate the utility of dynamic ALE for improving the conversion of mixed substrates into a single value-added product.

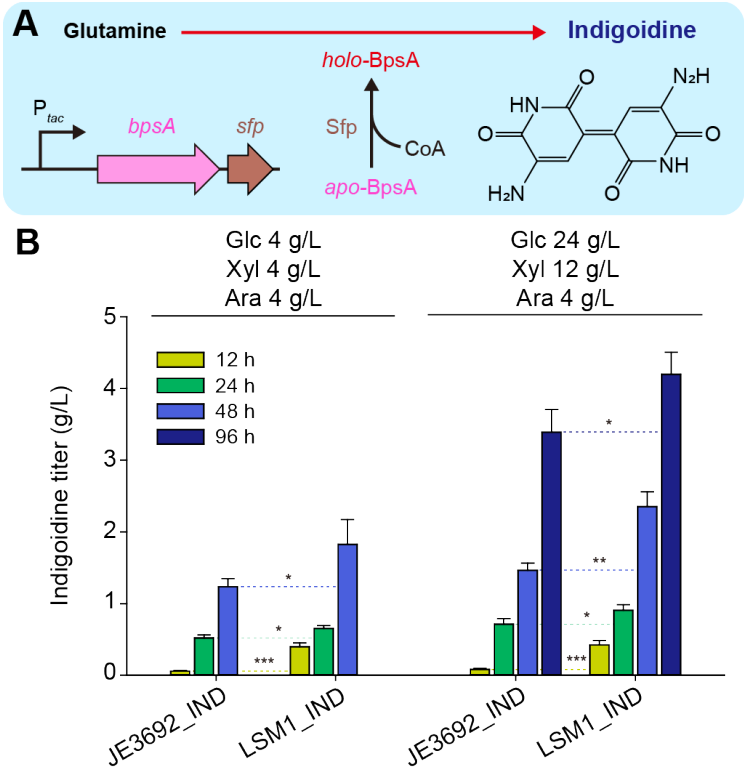

Figure 5. Indigoidine production from lignocellulosic sugars using evolved strain as a host

(A) The indigoidine production pathway in engineered *P. putida* strains. Indigoidine can be produced from glutamine by heterologous expression of *bpsA* from *S. lavendulae* and *sfp* from *B. subtilis*. These genes were expressed under the Tac promoter (P_{tac}) and the cassette was introduced into a plasmid. **(B)** Comparison of the indigoidine titers (g/L) of engineered strains based on the parental strain (JE3692) and an evolved strain (LSM1) after 12 h (yellow), 24 h (green), 48 h (blue), and 96 h (dark blue) cultivation under isotonic sugar condition (4 g/L of each sugar) and mock hydrolysate condition (24 g/L of glucose, 12 g/L of xylose, and 4 g/L of arabinose). The *x*- and *y*-axes indicate producer strain and indigoidine titer (g/L). *, ** and *** indicate statistical significance ($p < 0.05$, $p < 0.01$ and $p < 0.001$, respectively) between cultures of two different strains measured at the same timepoint. The cultures were conducted with biological triplicates ($n = 3$) and error bars indicate the standard deviations.

453 **Discussion**

454 In this study, we conducted an automated ALE campaign on a previously engineered *P. putida*
455 KT2440 strain, JE3692[23], under various dynamic selection regimes to optimize lignocellulosic
456 sugar catabolism. Statically evolved isolates generally exhibited improved growth relative to the
457 starting strain only under their respective selection conditions. Among dynamically evolved
458 isolates, those from the HSM and GXA regimes likewise evolved into catabolic specialists. In
459 contrast, LSM isolates, evolved under conditions that required complete consumption of all three
460 sugars, functioned as catabolic generalists with robust growth across single- and mixed-sugar
461 environments (**Figure 2B, E**). These findings indicate that LSM is an effective dynamic selection
462 regime for the simultaneous optimization of multi-sugar catabolism within a single ALE
463 experiment and provide a useful framework for developing robust microbial hosts for mixed-
464 carbon feedstock environments. Furthermore, the ALE-derived LSM1 strain led to improved
465 production of indigoidine demonstrating utility for biomanufacturing goals (**Figure 5B**).

466 The distinct mutational landscapes and variations in catabolic performance across dynamic ALE
467 regimes provided valuable insights into the rational design of evolutionary engineering strategies.
468 Interestingly, despite being evolved under the mixed-sugar conditions, the HSM isolates displayed
469 lower fitness than the LSM isolates when tested under the mixed-sugar conditions (**Figure 3D–E**).
470 This outcome likely reflects differences in sugar concentrations and transfer criteria during the
471 ALE experiments. Under the HSM mixed-sugar conditions, carbon remained abundant until
472 transfer, likely favoring early sweeps of sprinters that rapidly dominated the population by utilizing
473 easily catabolizable carbon sources[65]. However, such dynamics might not enforce sustained
474 selection for a high overall growth rate across the desired time frame for applications.
475 Consequently, HSM isolates often lost xylose catabolic ability that imposed fitness costs and
476 evolved as specialists on glucose and arabinose. These results provide a mechanistic example of
477 how fitness costs associated with specific catabolic pathways may contribute to hierarchical sugar
478 utilization in nutrient-rich and stable environments[10,11].

479 By contrast, LSM maintained low carbon availability and required complete sugar depletion before
480 transfer, imposing selection for efficient use of all three sugars and promoting generalists[65].
481 Furthermore, disruptive mutations in flagellar biosynthetic genes (*fliR* and *flgH*) and associated
482 regulatory genes (*fliA* and PP_5263 annotated as a GGDEF domain protein) in LSM isolates
483 (**Supplementary Data 1**) are likely attributed to more efficient proteome reallocation and reduced
484 motility or biofilm formation that increase specific growth rate[66,67]. Overall, these findings
485 emphasize the need to carefully and rationally design ALE conditions that preserve and co-
486 optimize targeted metabolic pathways while also accounting for factors such as mutation rates and
487 population sizes[39].

488 The investigation of selective disruption of the xylose catabolic pathway provided key insights
489 into metabolic pathway optimization and evolutionary engineering outcomes. Evolutionary
490 outcomes for the xylose pathway differed markedly between selective vs. non-selective regimes,
491 reflecting a balance between maintaining catabolic function and minimizing resource expenditure.
492 Under selective regimes, evolution appeared to prioritize reducing energy and resource burden
493 over preserving maximal catabolic activity. Conversely, under non-selective regimes, strains
494 frequently evolved with disruptions in the xylose pathway, likely due to the lack of selective
495 pressure to maintain catabolic activity and the fitness cost imposed by constitutively overexpressed

496 XylA and XylB. Consistent with our finding, several previous studies have reported that XylB
497 overexpression impairs cell fitness in *Saccharomyces cerevisiae* and *Corynebacterium*
498 *glutamicum*[68–70]. These divergent evolutionary outcomes highlight that evolutionary stability
499 arises from the combined effects of pathway design, enzyme specificity, functional efficiency, and
500 expression levels, which are especially important when optimizing multiple pathways.

501 This study represents a highly complex and parallelized ALE investigation, enabled by the use of
502 automated robotic ALEbot platforms. Prior plate-based automated ALE studies typically relied on
503 fixed schedules, such as transferring once per day or upon all cultures reaching a defined state,
504 which limited diverse selection regimes, particularly under regimes such as LSM and HSM[71,72]. In
505 this study, each lineage was cultivated in a separate tube, enabling individual OD tracking and
506 timely transfers that maintained consistent selective regimes and promoted distinct evolutionary
507 trajectories. Our results demonstrate that the dynamic ALE regime that enforced complete
508 consumption of all sugars can optimize multi-substrate catabolism, highlighting their advantage
509 over traditional static ALE that relies on a single selection pressure. Looking ahead, we expected
510 that this ALE-based dynamic selection strategy could be systematically applied to even more
511 complex and heterogeneous feedstocks, such as lignin-derived aromatics, marine polysaccharides,
512 and depolymerized mixed plastic waste[43,73–77].

513 **Methods**

514 **Bacterial strains, plasmids, and reagents**

515 Strains and plasmids used in this study are listed in **Supplementary Table 2**. Plasmids were
516 primarily constructed using the NEBuilder HiFi DNA Assembly Kit (New England Biolabs,
517 Ipswich, MA, USA). Oligonucleotides, synthesized by Integrated DNA Technologies (IDT,
518 Coralville, IA, USA), are listed in **Supplementary Table 3**. The plasmids used for recombination
519 were based on the pK18mobsacB backbone (ATCC 87097) and recombination regions either
520 cloned from isolates ARA3, LSM1, LSM2 or synthesized by GenScript (Piscataway, NJ, USA).
521 For DNA amplification, the Q5 High-Fidelity DNA polymerase or OneTaq DNA polymerase
522 (NEB) was used. Plasmids were purified using a Zymo PURE Plasmid Miniprep kit from Zymo
523 Research (Irvine, CA, USA). Genomic DNA samples were prepared by using a Quick-DNA
524 Fungal/Bacterial Miniprep kit from Zymo Research. Genome sequencing library samples were
525 prepared using an NEBNext Ultra II kit from NEB (Ipswich, MA, USA). All chemicals were
526 purchased from Sigma-Aldrich (St. Louis, MO, USA) and used without further purification.

527 **Culture conditions**

528 Bacterial cultivations were conducted in a Luria−Bertani (LB, 10 g/L tryptone, 5 g/L yeast extract,
529 10 g/L NaCl) or modified minimal M9 medium (4 g/L glucose, 2 g/L $(NH_4)_2SO_4$, 6.8 g/L Na_2HPO_4,
530 3 g/L KH_2PO_4, 0.5 g/L NaCl, 2 mM $MgSO_4$, 0.1 mM $CaCl_2$, 500 µL/L 2,000× trace element
531 solution). The composition of the trace element solution is 4.5 g/L $ZnSO_4 \cdot 7H_2O$, 0.7 g/L
532 $MnCl_2 \cdot 4H_2O$, 0.3 g/L $CoCl_2 \cdot 6H_2O$, 0.2 g/L $CuSO_4 \cdot 2H_2O$, 0.4 g/L $Na_2MoO_4 \cdot 2H_2O$, 4.5 g/L
533 $CaCl_2 \cdot 2H_2O$, 3.0 g/L $FeSO_4 \cdot 7H_2O$, 1.0 g/L H_3BO_3, 0.1 g/L KI, 15 g/L disodium
534 ethylenediaminetetraacetate[42,78]. For production strains only, gentamicin was supplemented at
535 30 µg/mL to maintain the plasmid carrying the indigoidine biosynthetic genes.

536 Cultures were performed in 30 mL cylindrical tubes containing 15 mL of medium at 30 °C, agitated
537 at 1,100 rpm with a magnetic stirring bar. Seed cultures were prepared by inoculating colonies
538 from LB agar plates into the minimal medium and incubating them overnight. Grown cultures
539 were diluted into the fresh medium at an OD_{600} of 0.1. When OD_{600} reached 0.6 ~ 1, cells were
540 harvested and re-inoculated into minimal media at OD_{600} of 0.05 to initiate experimental cultures.

541 For ALE, 150 µL of cultures at the late-exponential phase (OD_{600} of 0.6 ~ 1) were passed into
542 minimal medium supplemented with the indicated carbon sources, using an automated robotic
543 platform[39]. OD_{600} was measured using a Sunrise™ microplate reader from Tecan (Männedorf,
544 Switzerland). A maximum specific growth rate (h^{-1}) was calculated by linear regression between
545 ln(OD_{600}) and time (hour) during the exponential growth phase (OD_{600} ~ 1).

546 **Genome resequencing**

547 Raw sequencing reads were obtained by using a NovaSeq 6000 (Illumina) at the UC San Diego
548 IGM Genomics Center and analyzed by using Breseq (version 0.35.4)[79] and Bowtie2 (version
549 2.2.6)[80]. Mutations consistently present in the starting strain were filtered out (**Supplementary**
550 **Table 4**). Analysis results were uploaded to ALEdb v1.0[81] and are accessible at http://aledb.org
551 (project id: Pputida_dynamic_ALE). The summarized analysis results are also included in
552 **Supplementary Data 1**. Raw genome-sequencing files are available at the NCBI SRA database
553 (BioProject number: PRJNA1395279, **Supplementary Table 5**).

554 **Protein expression and purification**

555 Genes encoding XylA and XylB were cloned into a pET15b vector and transformed into *E. coli*
556 BL21(DE3). Cultures were grown at 37 °C in LB medium containing 50 µg/mL ampicillin until
557 reaching an OD_{600} of 0.6–0.8, at which point expression was induced with 1 mM IPTG and
558 continued overnight at 18 °C. Cells were harvested by centrifugation at 4,000 × *g* for 30 min at
559 4 °C, resuspended in lysis buffer (20 mM TRIS pH 8, 300 mM NaCl, 5 mM imidazole) and lysed
560 by sonication on ice. Lysates were clarified by centrifugation and purified using nickel affinity
561 chromatography (Ni-NTA IMAC). Eluted fractions were dialyzed (20 mM TRIS pH 8, 300 mM
562 NaCl), concentrated to >10 mg/mL, and flash frozen dropwise in liquid nitrogen, then stored at -
563 80 °C until use. XylA concentration was determined by absorbance at 280 nm using a calculated
564 extinction coefficient of 71,070 $M^{-1}cm^{-1}$, and XylB concentration was determined by absorbance
565 at 280 nm using a calculated extinction coefficient of 82,756 $M^{-1}cm^{-1}$.

566 **NMR analysis of XylA activity**

567 Reactions were performed in 100 mM potassium phosphate buffer (pH 8) containing 10 mM
568 $MgSO_4$, 20 mM sugar substrate (D-xylose, D-glucose, or L-arabinose), and 12 µM purified XylA.
569 Reaction mixtures (final volume: 600 µL) were supplemented to reach 10% D_2O and 0.1 mg/mL
570 TMSP (trimethylsilyl propionic acid) as an internal chemical shift and integration reference. ^1H
571 NMR spectra were acquired on a 400 MHz NMR spectrometer at room temperature using a
572 standard one-dimensional water-suppression pulse sequence. Spectra were processed and analyzed
573 in Mestrenova (Mestrelab Research). Product peaks for D-xylulose and D-fructose were identified
574 based on available published or reference spectra and quantified by peak integration. The L-
575 ribulose product lacked published assignments; thus, quantification was based on a representative

576 signal assumed to correspond to one or more protons (≥1 H). Final concentrations were estimated
577 using relative integration values calibrated to the TMSP internal standard.

578 **Coupled enzymatic assay to detect XylB activity**

579 XylB activity was monitored using a continuous, coupled assay with pyruvate kinase (PK) and
580 lactate dehydrogenase (LDH) linking ATP consumption to NADH oxidation. Reactions were
581 conducted in 200 mM potassium phosphate buffer (pH 8.0) supplemented with 20 mM $MgSO_4$, 2
582 mM phosphoenolpyruvate (PEP), 0.01X PK/LDH enzyme mix (with the 1X mixture
583 corresponding to ~600–1,000 U/mL pyruvate kinase and ~900–1400 U/mL LDH), 1 mM NADH,
584 and 0.04 µM purified XylB. Sugar substrates were added at 10 mM final concentration, except D-
585 xylulose, which was added at 2 mM. The final reaction volume was 200 µL and reactions were
586 performed in 96-well UV-STAR microplates (Greiner Bio-One). Absorbance at 340 nm (A_{340}) was
587 monitored at 1-minute intervals for 60 minutes at room temperature using a BioTek Synergy H1
588 plate reader.

589 **Proteome analysis**

590 *P. putida* cultures were collected after the OD_{600} reached 0.6 in minimal media supplemented with
591 4 g/L of glucose. Cells were harvested and stored at -80 °C until further processing. Protein was
592 extracted from cell pellets and tryptic peptides were prepared following the established proteomic
593 sample preparation protocol[82]. Briefly, cell pellets were resuspended in Qiagen P2 Lysis Buffer
594 (Qiagen, Germany) to promote cell lysis. Proteins were precipitated with the addition of 1 mM
595 NaCl and 4 x vol acetone, followed by two additional washes with 80% acetone in water. The
596 recovered protein pellet was homogenized by pipetting mixing with 100 mM ammonium
597 bicarbonate in 20% methanol. Protein concentration was determined by the DC protein assay
598 (BioRad, USA). Protein reduction was accomplished using 5 mM tris 2-(carboxyethyl)phosphine
599 (TCEP) for 30 min at room temperature, and alkylation was performed with 10 mM iodoacetamide
600 (IAM; final concentration) for 30 min at room temperature in the dark. Overnight digestion with
601 trypsin was accomplished with a 1:50 trypsin:total protein ratio.

602 The resulting peptide samples were analyzed on an Agilent 1290 UHPLC system coupled to a
603 Thermo Scientific Orbitrap Exploris 480 mass spectrometer for discovery proteomics[83]. Briefly,
604 peptide samples were loaded onto an Ascentis® ES-C18 Column (Sigma–Aldrich, USA) and were
605 eluted from the column by using a 10-minute gradient from 98% solvent A (0.1 % FA in H2O)
606 and 2% solvent B (0.1% FA in ACN) to 65% solvent A and 35% solvent B. Eluting peptides were
607 introduced to the mass spectrometer operating in positive-ion mode and were measured in data-
608 independent acquisition (DIA) mode with a duty cycle of 3 survey scans from m/z 380 to m/z 985
609 and 45 MS2 scans with precursor isolation width of 13.5 m/z to cover the mass range.

610 DIA raw data files were analyzed by the integrated software suite DIA-NN[84]. The databases used
611 in the DIA-NN search (library-free mode) are *P. putida* latest Uniprot proteome FASTA sequences
612 plus the protein sequences of the heterologous proteins and common proteomic contaminants.
613 DIA-NN determines mass tolerances automatically based on first pass analysis of the samples with
614 automated determination of optimal mass accuracies. The retention time extraction window was
615 determined individually for all MS runs analyzed via the automated optimization procedure
616 implemented in DIA-NN. Protein inference was enabled, and the quantification strategy was set
617 to Robust LC = High Accuracy. Output main DIA-NN reports were filtered with a global FDR =

0.01 on both the precursor level and protein group level. The Top3 method, which is the average MS signal response of the three most intense tryptic peptides of each identified protein, was used to plot the quantity of the targeted proteins in the samples[85,86]. The generated mass spectrometry proteomics data have been deposited to the ProteomeXchange Consortium via the PRIDE partner repository with the dataset identifier PXD055215[87]. The processed data and analysis results are provided in **Supplementary Data 2**. DIA-NN is freely available for download from https://github.com/vdemichev/DiaNN.

Metabolite quantification

Indigoidine was quantified after its extraction using dimethyl sulfoxide as described previously[56]. Absorbance at 612 nm was measured by using an Infinite® 200 PRO microplate reader from Tecan (Männedorf, Switzerland), and the concentration was determined from a calibration curve generated with indigoidine standards of known concentrations (**Supplementary Figure 9**). Concentrations of sugars were quantified by using a 1260 Infinity II LC system (Agilent, Santa Clara, CA, USA) equipped with an HPX-87H (Biorad, Hercules, CA, USA) and a refractive index detector. 5 mM H_2SO_4 was used as a mobile phase at a flow rate of 0.5 mL/min. The column temperature was maintained at 60 °C. A sugar consumption rate (g/L/h) was calculated by dividing the amount of sugar consumed (g/L) up to the late exponential phase by the corresponding cultivation time (h).

Acknowledgements

This material is based upon work at the Joint BioEnergy Institute supported by the U.S. Department of Energy, Office of Science, Biological and Environmental Research under Award Number DE-AC02-05CH11231. This work was also authored in part by the National Renewable Energy Laboratory for the U.S. Department of Energy (DOE) under Contract Number DE-AC36-08GO28308. Funding was provided to BNB, TML, CWJ, and GTB by the U.S. DOE Office of Energy Efficiency and Renewable Energy Bioenergy Technologies Office (BETO) Agile BioFoundry via Contract Number DE-AC36-08GO28308. This work was also authored in part by Oak Ridge National Laboratory, which is managed by UT-Battelle, LLC, for the U.S. Department of Energy (DOE) under Contract Number DE-AC05-00OR22725. Funding was provided to NG and AMG by the BETO Agile BioFoundry. The United States Government retains and the publisher, by accepting the article for publication, acknowledges that the United States Government retains a nonexclusive, paid-up, irrevocable, worldwide license to publish or reproduce the published form of this manuscript, or allow others to do so, for United States Government purposes. Any subjective views or opinions that might be expressed in this paper do not necessarily represent the views of the U.S. Department of Energy or the United States Government. H.G.L. acknowledges the National Research Foundation of Korea (NRF) grants funded by the Korea government (MSIT) (grant number RS-2024-00334792 and RS-2025-02215308). We thank Gayle Bentley and Lisa Guay at DOE and members of the Agile BioFoundry for helpful discussions. The purified indigoidine used in this study was kindly prepared by Javier Menasalvas. We thank Ciara de Venecia, Elina A. Olson, and Richard Szubin for technical support.

658 **References**

659 1. Zaldivar, J., Nielsen, J. & Olsson, L. Fuel ethanol production from lignocellulose: a challenge for
660 metabolic engineering and process integration. *Appl. Microbiol. Biotechnol.* **56**, 17–34 (2001).
661 2. Hahn-Hägerdal, B., Galbe, M., Gorwa-Grauslund, M. F., Lidén, G. & Zacchi, G. Bio-ethanol--the
662 fuel of tomorrow from the residues of today. *Trends Biotechnol.* **24**, 549–556 (2006).
663 3. Scheller, H. V. & Ulvskov, P. Hemicelluloses. *Annu. Rev. Plant Biol.* **61**, 263–289 (2010).
664 4. Chundawat, S. P. S., Beckham, G. T., Himmel, M. E. & Dale, B. E. Deconstruction of
665 lignocellulosic biomass to fuels and chemicals. *Annu. Rev. Chem. Biomol. Eng.* **2**, 121–145 (2011).
666 5. Keasling, J. *et al.* Microbial production of advanced biofuels. *Nat. Rev. Microbiol.* **19**, 701–715
667 (2021).
668 6. Han, T., Nazarbekov, A., Zou, X. & Lee, S. Y. Recent advances in systems metabolic engineering.
669 *Curr. Opin. Biotechnol.* **84**, 103004 (2023).
670 7. Ghoul, M. & Mitri, S. The ecology and evolution of microbial competition. *Trends Microbiol.* **24**,
671 833–845 (2016).
672 8. Bajic, D. & Sanchez, A. The ecology and evolution of microbial metabolic strategies. *Curr. Opin.*
673 *Biotechnol.* **62**, 123–128 (2020).
674 9. Machado, D. *et al.* Polarization of microbial communities between competitive and cooperative
675 metabolism. *Nat. Ecol. Evol.* **5**, 195–203 (2021).
676 10. Görke, B. & Stülke, J. Carbon catabolite repression in bacteria: many ways to make the most out of
677 nutrients. *Nat. Rev. Microbiol.* **6**, 613–624 (2008).
678 11. Wang, X., Xia, K., Yang, X. & Tang, C. Growth strategy of microbes on mixed carbon sources. *Nat.*
679 *Commun.* **10**, 1279 (2019).
680 12. Scott, M. & Hwa, T. Shaping bacterial gene expression by physiological and proteome allocation
681 constraints. *Nat. Rev. Microbiol.* **21**, 327–342 (2023).
682 13. Kim, J.-H., Block, D. E. & Mills, D. A. Simultaneous consumption of pentose and hexose sugars: an
683 optimal microbial phenotype for efficient fermentation of lignocellulosic biomass. *Appl. Microbiol.*

684 *Biotechnol.* **88**, 1077–1085 (2010).
685 14. Johnson, C. W. *et al.* Eliminating a global regulator of carbon catabolite repression enhances the
686 conversion of aromatic lignin monomers to muconate in *Pseudomonas putida* KT2440. *Metab. Eng.*
687 *Commun.* **5**, 19–25 (2017).
688 15. Liu, N., Santala, S. & Stephanopoulos, G. Mixed carbon substrates: a necessary nuisance or a missed
689 opportunity? *Curr. Opin. Biotechnol.* **62**, 15–21 (2020).
690 16. Nikel, P. I. & de Lorenzo, V. *Pseudomonas putida* as a functional chassis for industrial biocatalysis:
691 From native biochemistry to trans-metabolism. *Metab. Eng.* **50**, 142–155 (2018).
692 17. Weimer, A., Kohlstedt, M., Volke, D. C., Nikel, P. I. & Wittmann, C. Industrial biotechnology of
693 *Pseudomonas putida*: advances and prospects. *Appl. Microbiol. Biotechnol.* **104**, 7745–7766 (2020).
694 18. de Lorenzo, V., Pérez-Pantoja, D. & Nikel, P. I. *Pseudomonas putida* KT2440: the long journey of a
695 soil-dweller to become a synthetic biology chassis. *J. Bacteriol.* **206**, e0013624 (2024).
696 19. Meijnen, J.-P., de Winde, J. H. & Ruijssenaars, H. J. Engineering *Pseudomonas putida* S12 for
697 efficient utilization of D-xylose and L-arabinose. *Appl. Environ. Microbiol.* **74**, 5031–5037 (2008).
698 20. Meijnen, J.-P., de Winde, J. H. & Ruijssenaars, H. J. Establishment of oxidative D-xylose
699 metabolism in *Pseudomonas putida* S12. *Appl. Environ. Microbiol.* **75**, 2784–2791 (2009).
700 21. Dvořák, P. & de Lorenzo, V. Refactoring the upper sugar metabolism of *Pseudomonas putida* for co-
701 utilization of cellobiose, xylose, and glucose. *Metab. Eng.* **48**, 94–108 (2018).
702 22. Wang, Y. *et al.* Growth of engineered *Pseudomonas putida* KT2440 on glucose, xylose, and
703 arabinose: Hemicellulose hydrolysates and their major sugars as sustainable carbon sources. *Glob.*
704 *Change Biol. Bioenergy* **11**, 249–259 (2019).
705 23. Elmore, J. R. *et al.* Engineered *Pseudomonas putida* simultaneously catabolizes five major
706 components of corn stover lignocellulose: Glucose, xylose, arabinose, p-coumaric acid, and acetic
707 acid. *Metab. Eng.* **62**, 62–71 (2020).
708 24. Lim, H. G. *et al.* Generation of *Pseudomonas putida* KT2440 Strains with Efficient Utilization of
709 Xylose and Galactose via Adaptive Laboratory Evolution. *ACS Sustainable Chem. Eng.* **9**, 11512–

710 11523 (2021).
711 25. Dvořák, P. *et al.* Synthetically-primed adaptation of *Pseudomonas putida* to a non-native substrate
712 D-xylose. *Nat. Commun.* **15**, 2666 (2024).
713 26. Tiwari, R., Sathesh-Prabu, C., Kim, Y. & Kuk Lee, S. Simultaneous utilization of glucose and xylose
714 by metabolically engineered *Pseudomonas putida* for the production of 3-hydroxypropionic acid.
715 *Bioresour. Technol.* **395**, 130389 (2024).
716 27. Sandberg, T. E., Salazar, M. J., Weng, L. L., Palsson, B. O. & Feist, A. M. The emergence of
717 adaptive laboratory evolution as an efficient tool for biological discovery and industrial
718 biotechnology. *Metab. Eng.* **56**, 1–16 (2019).
719 28. Radek, A. *et al.* Miniaturized and automated adaptive laboratory evolution: Evolving
720 *Corynebacterium glutamicum* towards an improved d-xylose utilization. *Bioresour. Technol.* **245**,
721 1377–1385 (2017).
722 29. Mohamed, E. T. *et al.* Generation of an *E. coli* platform strain for improved sucrose utilization using
723 adaptive laboratory evolution. *Microb. Cell Fact.* **18**, 116 (2019).
724 30. Ling, C. *et al.* Muconic acid production from glucose and xylose in *Pseudomonas putida* via
725 evolution and metabolic engineering. *Nat. Commun.* **13**, 4925 (2022).
726 31. Woo, S. *et al.* A *Vibrio*-based microbial platform for accelerated lignocellulosic sugar conversion.
727 *Biotechnol Biofuels Bioprod* **15**, 58 (2022).
728 32. Huang, J. *et al.* Adaptive laboratory evolution and metabolic engineering of *Zymomonas mobilis* for
729 bioethanol production using molasses. *ACS Synth. Biol.* **12**, 1297–1307 (2023).
730 33. Woo, S. *et al.* Generation of a *Vibrio*-based platform for efficient conversion of raffinose through
731 Adaptive Laboratory Evolution on a solid medium. *Metab. Eng.* **86**, 300–307 (2024).
732 34. Sandberg, T. E., Lloyd, C. J., Palsson, B. O. & Feist, A. M. Laboratory Evolution to Alternating
733 Substrate Environments Yields Distinct Phenotypic and Genetic Adaptive Strategies. *Appl. Environ.*
734 *Microbiol.* **83**, (2017).
735 35. Kim, K. *et al.* Serial adaptive laboratory evolution enhances mixed carbon metabolic capacity of

736 *Escherichia coli*. *Metab. Eng.* **83**, 160–171 (2024).
737 36. Tai, Y.-S. *et al.* Engineering nonphosphorylative metabolism to generate lignocellulose-derived
738 products. *Nat. Chem. Biol.* **12**, 247–253 (2016).
739 37. Poblete-Castro, I. *et al.* In-silico-driven metabolic engineering of *Pseudomonas putida* for enhanced
740 production of poly-hydroxyalkanoates. *Metab. Eng.* **15**, 113–123 (2013).
741 38. Hernández-Arranz, S., Moreno, R. & Rojo, F. The translational repressor Crc controls the
742 *Pseudomonas putida* benzoate and alkane catabolic pathways using a multi-tier regulation strategy.
743 *Environ. Microbiol.* **15**, 227–241 (2013).
744 39. LaCroix, R. A., Palsson, B. O. & Feist, A. M. A Model for Designing Adaptive Laboratory
745 Evolution Experiments. *Appl. Environ. Microbiol.* **83**, (2017).
746 40. Lee, D.-H., Feist, A. M., Barrett, C. L. & Palsson, B. Ø. Cumulative number of cell divisions as a
747 meaningful timescale for adaptive laboratory evolution of *Escherichia coli*. *PLoS One* **6**, e26172
748 (2011).
749 41. Mohamed, E. T. *et al.* Adaptive laboratory evolution of *Pseudomonas putida* KT2440 improves p-
750 coumaric and ferulic acid catabolism and tolerance. *Metab Eng Commun* **11**, e00143 (2020).
751 42. Lim, H. G. *et al.* Generation of ionic liquid tolerant *Pseudomonas putida* KT2440 strains via
752 adaptive laboratory evolution. *Green Chem.* **22**, 5677–5690 (2020).
753 43. Werner, A. Z. *et al.* Adaptive laboratory evolution and genetic engineering improved terephthalate
754 utilization in *Pseudomonas putida* KT2440. *Metab. Eng.* **88**, 196–205 (2025).
755 44. Seo, S. W. *et al.* Predictive combinatorial design of mRNA translation initiation regions for
756 systematic optimization of gene expression levels. *Sci. Rep.* **4**, 4515 (2014).
757 45. Watanabe, S., Yamada, M., Ohtsu, I. & Makino, K. alpha-ketoglutaric semialdehyde dehydrogenase
758 isozymes involved in metabolic pathways of D-glucarate, D-galactarate, and hydroxy-L-proline.
759 Molecular and metabolic convergent evolution. *J. Biol. Chem.* **282**, 6685–6695 (2007).
760 46. Aghaie, A. *et al.* New insights into the alternative D-glucarate degradation pathway. *J. Biol. Chem.*
761 **283**, 15638–15646 (2008).

762 47. Wovcha, M. G., Steuerwald, D. L. & Brooks, K. E. Amplification of D-xylose and D-glucose
763 isomerase activities in *Escherichia coli* by gene cloning. *Appl. Environ. Microbiol.* **45**, 1402–1404
764 (1983).
765 48. Di Luccio, E. *et al.* Structural and kinetic studies of induced fit in xylulose kinase from *Escherichia*
766 *coli*. *J. Mol. Biol.* **365**, 783–798 (2007).
767 49. Fatima, B. & Javed, M. M. Production, purification and physicochemical characterization of D-
768 xylose/glucose isomerase from *Escherichia coli* strain BL21. *3 Biotech* **10**, 39 (2020).
769 50. Abramson, J. *et al.* Accurate structure prediction of biomolecular interactions with AlphaFold 3.
770 *Nature* **630**, 493–500 (2024).
771 51. Wilkes, R. A., Mendonca, C. M. & Aristilde, L. A cyclic metabolic network in *Pseudomonas*
772 *protegens* Pf-5 prioritizes the Entner-Doudoroff pathway and exhibits substrate hierarchy during
773 carbohydrate co-utilization. *Appl. Environ. Microbiol.* **85**, (2019).
774 52. Sudarsan, S., Dethlefsen, S., Blank, L. M., Siemann-Herzberg, M. & Schmid, A. The functional
775 structure of central carbon metabolism in *Pseudomonas putida* KT2440. *Appl. Environ. Microbiol.*
776 **80**, 5292–5303 (2014).
777 53. Chubukov, V., Gerosa, L., Kochanowski, K. & Sauer, U. Coordination of microbial metabolism.
778 *Nat. Rev. Microbiol.* **12**, 327–340 (2014).
779 54. Kern, A., Tilley, E., Hunter, I. S., Legisa, M. & Glieder, A. Engineering primary metabolic pathways
780 of industrial micro-organisms. *J. Biotechnol.* **129**, 6–29 (2007).
781 55. Zadeh, J. N. *et al.* NUPACK: Analysis and design of nucleic acid systems. *J. Comput. Chem.* **32**,
782 170–173 (2011).
783 56. Banerjee, D. *et al.* Genome-scale metabolic rewiring improves titers rates and yields of the non-
784 native product indigoidine at scale. *Nat. Commun.* **11**, 5385 (2020).
785 57. Wehrs, M. *et al.* Correction: Sustainable bioproduction of the blue pigment indigoidine: Expanding
786 the range of heterologous products in *R. toruloides* to include non-ribosomal peptides. *Green Chem.*
787 **21**, 6027–6029 (2019).

58. Wehrs, M. *et al.* Production efficiency of the bacterial non-ribosomal peptide indigoidine relies on the respiratory metabolic state in *S. cerevisiae*. *Microb. Cell Fact.* **17**, 193 (2018).

59. Ghiffary, M. R. *et al.* High-Level production of the natural blue pigment indigoidine from metabolically engineered *Corynebacterium glutamicum* for sustainable fabric dyes. *ACS Sustain. Chem. Eng.* **9**, 6613–6622 (2021).

60. Takahashi, H. *et al.* Cloning and characterization of a *Streptomyces* single module type non-ribosomal peptide synthetase catalyzing a blue pigment synthesis. *J. Biol. Chem.* **282**, 9073–9081 (2007).

61. Owen, J. G., Copp, J. N. & Ackerley, D. F. Rapid and flexible biochemical assays for evaluating 4'-phosphopantetheinyl transferase activity. *Biochem. J.* **436**, 709–717 (2011).

62. Bagdasarian, M. M., Amann, E., Lurz, R., Rückert, B. & Bagdasarian, M. Activity of the hybrid trp-lac (tac) promoter of *Escherichia coli* in *Pseudomonas putida*. Construction of broad-host-range, controlled-expression vectors. *Gene* **26**, 273–282 (1983).

63. Johnson, C. W. & Beckham, G. T. Aromatic catabolic pathway selection for optimal production of pyruvate and lactate from lignin. *Metab. Eng.* **28**, 240–247 (2015).

64. Chen, X. *et al.* DMR (deacetylation and mechanical refining) processing of corn stover achieves high monomeric sugar concentrations (230 g L−1) during enzymatic hydrolysis and high ethanol concentrations (>10% v/v) during fermentation without hydrolysate purification or concentration. *Energy Environ. Sci.* **9**, 1237–1245 (2016).

65. Marshall, D. J., Cameron, H. E. & Loreau, M. Relationships between intrinsic population growth rate, carrying capacity and metabolism in microbial populations. *ISME J.* **17**, 2140–2143 (2023).

66. Honda, T. *et al.* Coordination of gene expression with cell size enables *Escherichia coli* to efficiently maintain motility across conditions. *Proc. Natl. Acad. Sci. U. S. A.* **119**, e2110342119 (2022).

67. Maughan, H. & Nicholson, W. L. Increased fitness and alteration of metabolic pathways during *Bacillus subtilis* evolution in the laboratory. *Appl. Environ. Microbiol.* **77**, 4105–4118 (2011).

68. Jin, Y.-S., Ni, H., Laplaza, J. M. & Jeffries, T. W. Optimal growth and ethanol production from

814 xylose by recombinant *Saccharomyces cerevisiae* require moderate D-xylulokinase activity. *Appl.*
815 *Environ. Microbiol.* **69**, 495–503 (2003).
816 69. Johansson, B., Christensson, C., Hobley, T. & Hahn-Hägerdal, B. Xylulokinase overexpression in
817 two strains of *Saccharomyces cerevisiae* also expressing xylose reductase and xylitol dehydrogenase
818 and its effect on fermentation of xylose and lignocellulosic hydrolysate. *Appl. Environ. Microbiol.*
819 **67**, 4249–4255 (2001).
820 70. Radek, A. *et al.* Formation of xylitol and xylitol-5-phosphate and its impact on growth of d-xylose-
821 utilizing *Corynebacterium glutamicum* strains. *J. Biotechnol.* **231**, 160–166 (2016).
822 71. Lukačišinová, M., Fernando, B. & Bollenbach, T. Highly parallel lab evolution reveals that epistasis
823 can curb the evolution of antibiotic resistance. *Nat. Commun.* **11**, 3105 (2020).
824 72. Hirasawa, T. & Maeda, T. Adaptive laboratory evolution of microorganisms: Methodology and
825 application for bioproduction. *Microorganisms* **11**, 92 (2022).
826 73. Aristidou, A. & Penttilä, M. Metabolic engineering applications to renewable resource utilization.
827 *Curr. Opin. Biotechnol.* **11**, 187–198 (2000).
828 74. Sasaki, Y. & Yoshikuni, Y. Metabolic engineering for valorization of macroalgae biomass. *Metab.*
829 *Eng.* **71**, 42–61 (2022).
830 75. Sullivan, K. P. *et al.* Mixed plastics waste valorization through tandem chemical oxidation and
831 biological funneling. *Science* **378**, 207–211 (2022).
832 76. Werner, A. Z. *et al.* Lignin conversion to β-ketoadipic acid by *Pseudomonas putida* via metabolic
833 engineering and bioprocess development. *Sci. Adv.* **9**, eadj0053 (2023).
834 77. Weiland, F., Kohlstedt, M. & Wittmann, C. Guiding stars to the field of dreams: Metabolically
835 engineered pathways and microbial platforms for a sustainable lignin-based industry. *Metab. Eng.*
836 **71**, 13–41 (2022).
837 78. Mohamed, E. T. *et al.* Generation of a platform strain for ionic liquid tolerance using adaptive
838 laboratory evolution. *Microb. Cell Fact.* **16**, 204 (2017).
839 79. Deatherage, D. E. & Barrick, J. E. Identification of mutations in laboratory-evolved microbes from

840 next-generation sequencing data using breseq. *Methods Mol. Biol.* **1151**, 165–188 (2014).
841 80. Langmead, B. & Salzberg, S. L. Fast gapped-read alignment with Bowtie 2. *Nat. Methods* **9**, 357–
842 359 (2012).
843 81. Phaneuf, P. V., Gosting, D., Palsson, B. O. & Feist, A. M. ALEdb 1.0: a database of mutations from
844 adaptive laboratory evolution experimentation. *Nucleic Acids Res.* **47**, D1164–D1171 (2019).
845 82. Chen, Y. Alkaline-SDS cell lysis of microbes with acetone protein precipitation for proteomic
846 sample preparation in 96-well plate format v1. (2021) doi:10.17504/protocols.io.6qpvr6xjpvmk/v1.
847 83. Chen, Y., Gin, J. & J Petzold, C. Discovery proteomic (DIA) LC-MS/MS data acquisition and
848 analysis v2. (2022) doi:10.17504/protocols.io.e6nvwk1z7vmk/v2.
849 84. Demichev, V., Messner, C. B., Vernardis, S. I., Lilley, K. S. & Ralser, M. DIA-NN: neural networks
850 and interference correction enable deep proteome coverage in high throughput. *Nat. Methods* **17**, 41–
851 44 (2020).
852 85. Ahrné, E., Molzahn, L., Glatter, T. & Schmidt, A. Critical assessment of proteome-wide label-free
853 absolute abundance estimation strategies. *Proteomics* **13**, 2567–2578 (2013).
854 86. Silva, J. C., Gorenstein, M. V., Li, G.-Z., Vissers, J. P. C. & Geromanos, S. J. Absolute
855 quantification of proteins by LCMSE. *Mol. Cell. Proteomics* **5**, 144–156 (2006).
856 87. Perez-Riverol, Y. *et al.* The PRIDE database resources in 2022: a hub for mass spectrometry-based
857 proteomics evidences. *Nucleic Acids Res.* **50**, D543–D552 (2022).